A Unified Numerical Modeling of Stationary Tungsten-Inert-Gas Welding Process

MANABU TANAKA, HIDENORI TERASAKI, MASAO USHIO, and JOHN J. LOWKE

In order to clarify the formative mechanism of weld penetration in an arc welding process, the development of a numerical model of the process is quite useful for understanding quantitative values of the balances of mass, energy, and force in the welding phenomena because there is still lack of experimentally understanding of the quantitative values of them because of the existence of complicated interactive phenomena between the arc plasma and the weld pool. The present article is focused on a stationary tungsten-inert-gas (TIG) welding process for simplification, but the whole region of TIG arc welding, namely, tungsten cathode, arc plasma, workpiece, and weld pool is treated in a unified numerical model, taking into account the close interaction between the arc plasma and the weld pool. Calculations in a steady state are made for stationary TIG welding in an argon atmosphere at a current of 150 A. The anode is assumed to be a stainless steel, SUS304, with its negative temperature coefficient of surface tension. The two-dimensional distributions of temperature and velocity in the whole region of TIG welding process are predicted. The weld-penetration geometry is also predicted. Furthermore, quantitative values of the energy balance for the various plasma and electrode regions are given. The predicted temperatures of the arc plasma and the tungsten-cathode surface are in good agreement with the experiments. There is also approximate agreement of the weld shape with experiment, although there is a difference between the calculated and experimental volumes of the weld. The calculated convective flow in the weld pool is mainly dominated by the drag force of the cathode jet and the Marangoni force as compared with the other two driving forces, namely, the buoyancy force and the electromagnetic force.

I. INTRODUCTION

HEAT transfer from the arc plasma to the weld pool plays an important role in the determination of the weld penetration in the arc-welding process.[1] Details of the fluid flow in the weld pool are important in determining weld shape. Taking account of all these phenomena is necessary for the development of a numerical model of the tungsten-inert-gas (TIG) welding process because there is close interaction between the arc plasma and the weld pool. For example, there are four driving forces of fluid flow in the weld pool.[2] These are the drag force of the cathode jet on the liquid surface, the buoyancy force, the electromagnetic force due to the self-magnetic field of the welding current, and the surface-tension gradient force of the weld pool, as shown in Figure 1.[2] These driving forces are dependent not only on the physical properties of the weld metal but also the properties of the plasma state.[1] Therefore, a unified numerical model accounting for both plasma and weld-metal processes is important for predicting the TIG arc-welding properties.

Modeling the arc-welding process has been tried by a number of researchers.[2–15] However, almost every numerical model has treated either only the arc plasma[3–8] or only the weld pool.[2,9–13] Then, calculated predictions, for example, for the weld pool, require distributions of heat flux and current density to be specified at the anode surface. Recently, modeling the combined arc plasma and the weld-pool phenomena has been tried for stationary welding,[14,15] but the calculated results of the arc plasma and the weld pool were made separately, without interaction between the plasma and the weld pool.

In the present article, we use a unified numerical model of stationary TIG arc welding. The basic model and procedure is that of Sansonnens *et al.*[16] but it is extended to include melting of the anode, with inclusion of convective effects in the weld pool. We give predictions of the two-dimensional distributions of temperature and velocity in the whole region of the TIG welding process and also the predicted profile of weld penetration. Furthermore, quantitative values of the energy balance for the various plasma and electrode regions are given. We did not take into consideration the metal-vapor phenomenon from the weld pool and depression of the weld-pool surface.

II. MODEL OF TIG WELDING PROCESS

A. *Governing Equations*

The tungsten cathode, arc plasma, and anode are described relative to a cylindrical coordinate, assuming rotational symmetry around the arc axis. The calculation domain is shown in Figure 2. The domain of computation is divided into 95 nodes axially and 70 nodes radially, using a nonuniform grid. The flow is assumed to be laminar, the electron and heavy particle temperature are assumed to be equal, and the effects of the noncollisional space-charged zone in front of both electrodes are neglected. Furthermore, the anode surface is assumed to be flat and unperturbed by the arc pressure.

MANABU TANAKA, Research Associate, HIDENORI TERASAKI, Ph.D Student, and MASAO USHIO, Professor, are with the Joining and Welding Research Institute, Osaka University, Osaka 567-0047, Japan. Contact e-mail: tanaka@jwri.osaka-u.ac.jp JOHN J. LOWKE, Chief Research Scientist, is with the Department of Telecommunications and Industrial Physics, CSIRO, Lindfield, NSW 2070, Australia.

Manuscript submitted November 1, 2001.

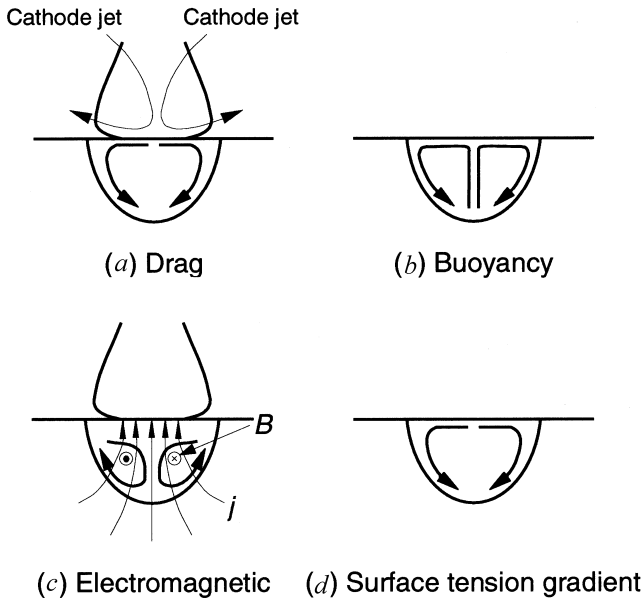

Fig. 1—(*a*) through (*d*) Flow directions induced by four possible driving forces in the weld pool.

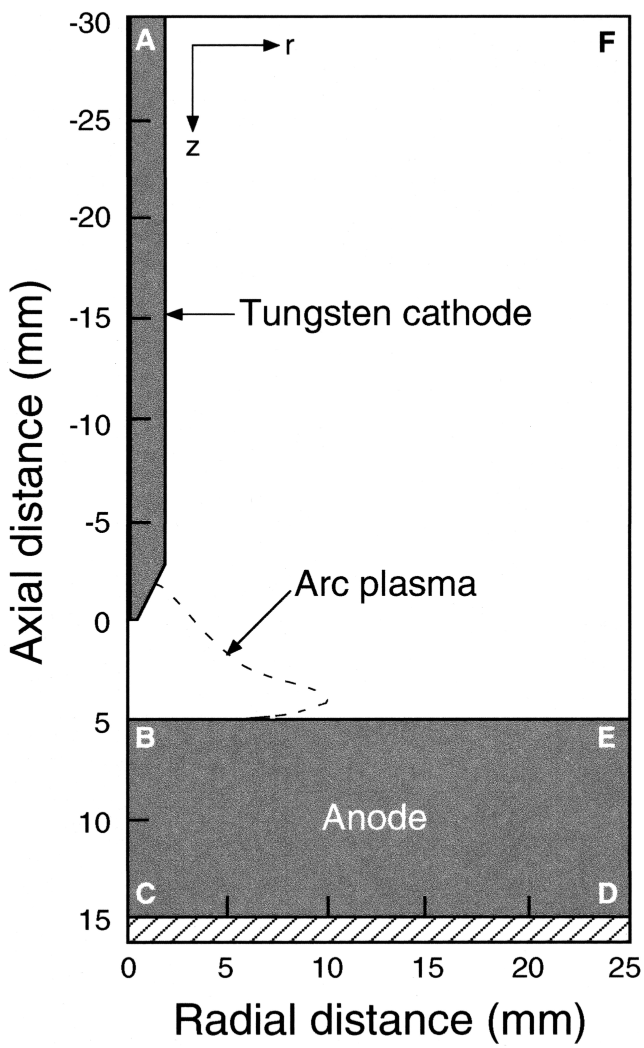

Fig. 2—Schematic illustration of calculated domain.

The diameter of the tungsten cathode is 3.2 mm with a 60-deg conical tip. The metal vapor from the weld pool is neglected in this model. The shielding gas of the TIG welding process is assumed to be pure argon.

The governing equations are given in Sansonnens *et al.*[16] and then only the most pertinent details are explained here. The mass-continuity equation is

$$\frac{1}{r}\frac{\partial}{\partial r}(r\rho v_r) + \frac{\partial}{\partial r}(\rho v_z) = 0. \quad [1]$$

The radial-momentum conservation equation is

$$\frac{1}{r}\frac{\partial}{\partial r}(r\rho v_r^2) + \frac{\partial}{\partial z}(\rho v_z v_r) = -\frac{\partial P}{\partial r} - j_z B_\theta + \frac{1}{r}\frac{\partial}{\partial r}\left(2r\eta\frac{\partial v_r}{\partial r}\right) + \frac{\partial}{\partial z}\left(\eta\frac{\partial v_r}{\partial z} + \eta\frac{\partial v_z}{\partial r}\right) - 2\eta\frac{v_r}{r^2} \quad [2]$$

The axial-momentum conservation equation is

$$\frac{1}{r}\frac{\partial}{\partial r}(r\rho v_r v_z) + \frac{\partial}{\partial z}(\rho v_z^2) = -\frac{\partial P}{\partial z} + j_r B_\theta + \frac{\partial}{\partial z}\left(2\eta\frac{\partial v_z}{\partial z}\right) + \frac{1}{r}\frac{\partial}{\partial r}\left(r\eta\frac{\partial v_r}{\partial z} + r\eta\frac{\partial v_z}{\partial r}\right) + \rho g \quad [3]$$

The energy-conservation equation is

$$\frac{1}{r}\frac{\partial}{\partial r}(r\rho v_r h) + \frac{\partial}{\partial z}(\rho v_z h) = \frac{1}{r}\frac{\partial}{\partial r}\left(\frac{r\kappa}{c_p}\frac{\partial h}{\partial r}\right) + \frac{\partial}{\partial z}\left(\frac{\kappa}{c_p}\frac{\partial h}{\partial z}\right) + j_r E_r + j_z E_z - U \quad [4]$$

The current-continuity equation is

$$\frac{1}{r}\frac{\partial}{\partial r}(r j_r) + \frac{\partial}{\partial z}(j_z) = 0 \quad [5]$$

where h is enthalpy, P is pressure, v_z and v_r are the axial and radial velocities, j_z and j_r are the axial and radial component of the current density, g is the acceleration due to gravity, κ is the thermal conductivity, c_p is the specific heat, ρ is the density, η is the viscosity, U is the radiation emission coefficient, E_r and E_z are, respectively, the radial and axial components of the electric field defined by $E_r = -\partial V/\partial r$ and $E_z = -\partial V/\partial z$, where V is electric potential.

Instead of the usual representation of the current density as dependent only on the electric field by Ohm's law ($j = \sigma E$, where σ is the electrical conductivity), we also include a term to account for diffusion current from electrons. This term overcomes the problem that the equilibrium electrical conductivity is effectively zero in the plasma close to the electrodes owing to the low plasma temperature. This diffusion term is also consistent with our previous article, which suggested that the diffusion current would dominate the arc current in the anode boundary layer.[17] Thus,

$$j_r = -\sigma\frac{\partial V}{\partial r} + eD_e\frac{\partial n_e}{\partial r} \quad [6]$$

and

$$j_z = -\sigma\frac{\partial V}{\partial z} + eD_e\frac{\partial n_e}{\partial z} \quad [7]$$

where D_e is the electron-diffusion coefficient, e is the elementary charge, and n_e is the electron-number density. The azimuthal-magnetic field, B_θ, induced by the arc current is evaluated by Maxwell's equation,

$$\frac{1}{r}\frac{\partial}{\partial r}(rB_\theta) = \mu_0 j_z \qquad [8]$$

where μ_0 is the permeability of free space. The electron-continuity equation in terms of ambipolar diffusion is

$$\frac{1}{r}\frac{\partial}{\partial r}\left(rD_{\text{amb}}\frac{\partial n_e}{\partial r}\right) + \frac{\partial}{\partial z}\left(D_{\text{amb}}\frac{\partial n_e}{\partial z}\right) + \gamma[K_{eq}(T)\, n_e n_a - n_e^3] = 0 \qquad [9]$$

where D_{amb} is the ambipolar coefficient evaluated using the data of Devoto,[18,19] $K_{eq}(T)$ is the Saha function, T is temperature, γ is the three-body recombination coefficient,[20,21] and n_0 is the neutral number density.

B. *Electrode Surfaces*

Calculations at points on the cathode surface would need to include the special process occurring at the surface. Thus, additional energy-flux terms need to be included in Eq. [4] at the cathode surface for thermionic cooling from the cathode, ion heating, and radiation cooling. The additional energy flux for the cathode, H_K is

$$\text{Cathode } H_\kappa = -\varepsilon\alpha T^4 - |j_e|\phi_K + |j_i|V_i \qquad [10]$$

where ε is the surface emissivity, α is the Stefan–Boltzmann constant, ϕ_K is the work function of the tungsten cathode, V_i is the ionization potential of argon, j_e is the electron-current density, and j_i is the ion-current density. At the cathode surface and for thermionic emission of electrons, j_e cannot exceed the Richardson current density, j_R, given by

$$|j_R| = AT^2 \exp\left(-\frac{e\phi_e}{k_B T}\right) \qquad [11]$$

where A is the thermionic-emission constant for the surface of the cathode, ϕ_e is the effective work function for thermionic emission of the electrode surface at the local surface temperature, and k_B is the Boltzmann's constant. The ion-current density, j_i, is then assumed to be $|j| - |j_R|$ if $|j|$ is greater than $|j_R|$; where $|j| = |j_e| + |j_i|$ is the total current density at the cathode surface obtained from Eq. [5].

Calculations at points on the anode surface would also need to include the special process occurring at the surface. The additional energy-flux terms need to be included in Eq. [4] at the anode surface for thermionic heating and radiation cooling. The additional energy flux for the anode, H_A, is

$$\text{Anode } H_A = -\varepsilon\alpha T^4 + |j|\phi_A \qquad [12]$$

where ϕ_A is the work function of the anode, and $|j|$ is the current density at the anode surface obtained from Eq. [5]. In most cases, it has been considered that the heat transfer to the anode needs to include more additional terms into Eq. [12] for anode-fall heating, $j \cdot V_A$, and electron enthalpy entering the anode, $j(5/2(k_B T_e/e))$.[22,23] Here, V_A is the anode fall, and T_e is the electron temperature. The $j \cdot V_A$ means electron heating accelerated by the V_A without collisions in the plasma. However, the anode fall in the arc plasma is widely distributed in comparison with the mean-free-path length of electrons,[17,24] and then electron-ion collision or electron-neutral atom collision should occur in the anode-fall region. Therefore, taking into account simply the $j \cdot V_A$ term would overestimate the energy flux into the anode. We think that the $j \cdot V_A$ term is already included in Eq. [4] because the energy of electron heating accelerated by the V_A changes "temperature" by sufficient collisions in the anode-fall region. The effect of the $j(5/2(k_B T_e/e))$ term on the anode heat transfer would depend on properties of the plasma state, particularly, arc current.[25] In the case of high current arc, plasma close to the anode still preserves a state similar to the local thermodynamic equilibrium (LTE), and the negative anode fall would reduce the electron temperature. Thus, the $j(5/2(k_B T_e/e))$term becomes small. In the case of low current arc, plasma remarkably deviates from LTE, and the positive anode fall heats the electron, and then the $j(5/2(k_B T_e/e))$ term becomes important. The arc current is assumed to be 150 A in the present article, and it is seen to be sufficient high current.[25] Thus, it is safe to take no account of the $j(5/2(k_B T_e/e))$ term in Eq. [12], and it would be assumed that the $j(5/2(k_B T_e/e))$ term is reflected in the general enthalpy of the argon-arc plasma in Eq. [4], owing to sufficient collisions of electron-ion and electron-neutral atom in the plasma. A two-temperature model of the arc plasma, namely, a model of nonequilibrium plasma[26] would be necessary for taking the $j(5/2(k_B T_e/e))$ term into account.

At the anode surface, BE in Figure 2, there are two sources of radial momentum, as shown in Figure 1. The first is the drag force, namely, the shear stress that is applied by the cathode jet on the surface of the weld pool, and the second is the surface-tension gradient force, namely, the Marangoni force. The drag force is already reflected in Eq. [2] for the radial-momentum conservation. The viscosity, η, makes the drag force at the anode surface. Therefore, the Marangoni force would need to be included in the radial-momentum conservation at points on the anode surface, BE. In most cases, the difference in surface tension arises from the temperature variation at the weld-pool surfaces,[10] and then the Marangoni force, τ, can be expressed by

$$\tau = -\eta\frac{\partial v_r}{\partial z} = \frac{\partial \gamma}{\partial T}\frac{\partial T}{\partial r} \qquad [13]$$

where γ is the surface tension of the weld pool. Therefore, the additional term for Eq. [2] at the anode surface, F_A, is

$$\text{Anode } F_A = \frac{\partial}{\partial z}\left(\frac{\partial \gamma}{\partial T}\frac{\partial T}{\partial r}\right) \qquad [14]$$

In the present article, we assumed that the anode was a stainless steel SUS304 and the surface tension of molten SUS304 linearly decreased with temperature increase, as shown in Figure 3.[9]. However, we were able to change the anode materials easily, and then we also used a copper as the anode for some comparisons with experiments, for example, comparisons of the energy loss and the plasma temperature with those values of experiments.

C. *Boundary Conditions and Numerical Method*

The detailed boundary conditions and numerical method are also given in Sansonnens *et al.*,[16] however, only the most pertinent points are outlined here.

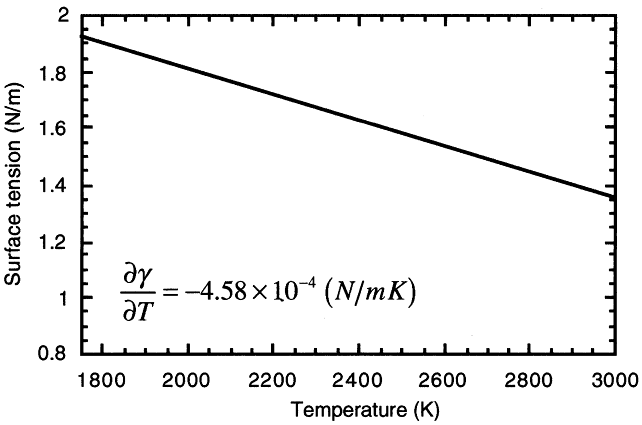

Fig. 3—Assumption of surface tension of molten SUS304.

Within both the electrodes, namely, cathode and anode, we set $v_r = v_z = 0$. However, in the anode, both the velocities, namely, v_r and v_z are calculated by Eq. [2] at the region in which temperature is more than the melting point of SUS304. Furthermore, we set $v_z = 0$ at the anode surface, BE, in Figure 2. The temperatures at boundaries CD, DE, EF, and FA in Figure 2 are taken to be the same room temperature, namely, 300 K.

Within both the electrodes, we set n_e and D_e to zero. We also set $n_e = 0$ at the anode surface, corresponding to an absorbing surface. However, at the cathode surface, we determine a boundary value for n_e from $j_R = en_e v_{th}$; j_R is calculated from Eq. [11], and v_{th} is the mean speed of emitted electrons taken here to be equal to the thermal velocity $(8k_BT/\pi m_e)^{1/2}$.[27]

The differential Eq. [1] to [9] of Patankar are solved iteratively by using the numerical procedure.[28] Major physical properties used in this model are listed in Table I.[29–32]

III. EXPERIMENTAL METHOD

A stationary TIG welding was performed for comparison of the weld penetration with a calculated result. The experimental setup is shown in Figure 4. The experiment was made for 20 seconds of arcing, so that conditions were then in the steady state, to be comparable to the results of the steady state calculation. We took the short time of 20s for arcing to avoid effects, for example, due to evaporation of surface active elements such as sulfur and oxygen from the weld pool, which would vary the surface tension coefficient. The anode was a disk (50 mm in diameter and 10 mm in thickness) of SUS304 that was mounted into the water-cooled copper wall. The W-2 pct La_2O_3 electrode (diameter 3.2 mm with a conical tip angle of 60 deg) was used with a 5-mm arc length. The argon was employed as shielding gas at flow rate of 15 l/min.

IV. RESULTS AND DISCUSSIONS

Figure 5 represents a two-dimensional distribution of temperature in the whole region of the stationary TIG welding of SUS304 for a 150 A in welding current. The maximum temperatures of the tungsten cathode, arc plasma, and weld pool are ~3500 K at the tip of the cathode, 17,000 K on the arc axis close to the cathode tip, and 2000 K at the center of the anode surface, respectively. Figure 6 represents a two-dimensional distribution of fluid-flow velocity. The interaction of the arc current with its own magnetic field leads to the phenomena of induced mass flow from the cathode to the anode. This induced mass flow is generally called the cathode jet.[22] The maximum calculated velocity of the cathode jet reaches 203 ms^{-1}. Snyder showed an experimental result of axial velocity in argon TIG arc by using the laser-scattering measurement.[33] His result showed that the cathode-jet velocity reached around 300 ms^{-1} for 200 A in arc current. In the case of 150 A in arc current, 100 to 200 ms^{-1} in the cathode-jet velocity was reviewed.[34] Therefore, our calculated result of the cathode-jet velocity is in good agreement with the experimental results. This axial fluid flow of the cathode jet changes its direction in front of the anode surface, and then, its radial component of the fluid flow drags the surface of the weld pool. This drag force is one of the driving forces of outward fluid flow in the weld pool. The outward fluid flow is also caused by a negative temperature coefficient of surface tension, assumed in Figure 3. The fluid flow caused by the surface-tension gradient force is called the Marangoni convection. Figure 7 shows distributions of temperature and fluid-flow velocity of the weld for the individual driving forces corresponding to Figure 1. These calculations were made under the same conditions as Figures 5 and 6. Each maximum velocity for drag, buoyancy, electromagnetic, and Marangoni force is 47, 1.4, 4.9 and 18 cm s^{-1}, respectively. Each value except for the drag force is similar to the calculated results by Choo and Szekely.[14] Unfortunately, their numerical calculations did not include the drag force effect at the weld-pool surface. Figure 7 suggests that the calculated convective flow in the weld pool is mainly dominated by the drag force of the cathode jet and the Marangoni force as compared with other two driving forces, namely, the buoyancy force and the electromagnetic force. Figure 6 represents a numerical result corresponding to outward fluid flow with a wide and shallow weld penetration that is a typical geometry in the TIG arc-welding process. The maximum calculated velocity in the weld pool for all considered cases reaches 54 cms^{-1}, as shown in Figure 6. Choo and Szekely showed that a maximum surface velocity in the weld pool was around 40 cms^{-1} for 100 A in welding current.[14] Furthermore, Goodarzi showed that a maximum surface velocity was 36.2 cms^{-1} for 200 A in welding current,[15] and Winkler also showed that it reached 68 cms^{-1} for 100 A.[13] Therefore, our calculated result of the surface velocity of the weld pool is similar to previously calculated results shown in other articles. However, this small difference would lead to the differences in the heat and mass transfer in the weld pool and then bring visible differences into the weld-penetration geometry.

Figure 8 shows components of the whole energy balance in TIG arc welding. Table II shows numerical results for calculation of energy balances in the case of the same conditions as Figures 5 and 6. Ohmic heating of 47, 1183, and 1 W occurs in the cathode, arc plasma, and anode, respectively. The ohmic heating in the arc plasma reaches 97 pct of the total heating in TIG arc welding. The total heating is a product of the welding current, 150 A, multiplied by the welding voltage, 8.1 V. The welding voltage, as shown in Figure 2, is given by the electric potential at the cathode top, A, with respect to the anode bottom, CD, which is

Table I. Major Physical Properties Used in This Model

Physical properties of cathode, arc plasma, and anode		
Cathode	work function	4.52 V
	effective work function for thermionic emission	2.63 V
	thermionic emission constant for Richardson equation	3.0 A/cm^2 K^2
	thermal conductivity	2.40 to 0.85 W/cm K
	electrical conductivity	2.2×10^5 to 5.9×10^3 A/V cm
	specific heat	0.13 to 0.22 J/g K
	density	18.9 g/cm^3
Arc plasma	ionization potential of argon	15.68 V
	thermal conductivity	1.8×10^{-4} to 2.7×10^{-2} W/cm K
	electrical conductivity	1.0×10^{-4} to 1.0×10^2 A/V cm
	specific heat	0.52–9.3 J/g K
	density	1.6×10^{-3} to 1.2×10^{-5} g/cm^3
	viscosity	2.3×10^{-4} to 2.6×10^{-3} g/cm s
Anode (SUS304)	melting point	1750 K
	work function	4.65 V
	thermal conductivity	0.12 to 0.30 W/cm K
	electrical conductivity	1.4×10^4 to 6.9×10^3 A/V cm
	specific heat	0.51 to 0.65 J/g K
	density	7.9 to 7.8 g/cm^3
	viscosity	6.0×10^{-2} to 1.5×10^{-2} g/cm s
Anode (Cu)	melting point	1353 K
	work function	4.65 V
	thermal conductivity	4.33 to 2.7 W/cm K
	electrical conductivity	1.2×10^6 to 7.5×10^4 A/V cm
	specific heat	0.37 to 0.50 J/g K
	density	8.9 g/cm^3
	viscosity	4.0 to 1.6 g/cm s

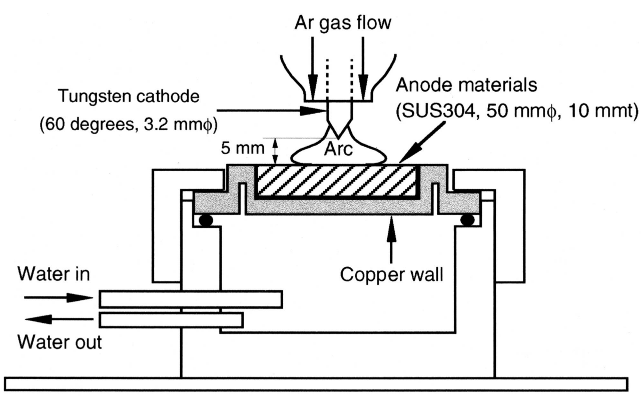

Fig. 4—Schematic illustration of the apparatus for stationary TIG welding of SUS304.

earthed. Most of the generated thermal energy by the ohmic heating in the arc plasma is transferred to the cathode and anode, with the remaining energy disappearing as energy loss by radiation. A heat flux of 478 W for thermal conduction and 156 W for neutralization of the ion flux are transferred from the arc to the tungsten cathode. A heat flux of 373 W for thermal conduction is transferred from the arc to the anode. The energy loss by radiation and conduction from the arc plasma is 276 and 5 W, respectively. The energy loss from the cathode consists of the thermionic emission of electrons, 678 W; thermal conduction, 33 W; and radiation, 47 W; and it balances against the energy input from the arc plasma, as mentioned previously. The energy loss from the anode consists of the conduction to the anode bottom, 1009 W, and radiation, 30 W. This loss is balanced by the energy input from the arc plasma, which consists of the electron absorption at the anode surface ($j\phi_A$), 697 W, and thermal conduction, 373 W. It is suggested that the anode heat transfer from the arc plasma, in this condition of 150 A in welding current, is dominated by the energy of electron absorption at the anode surface as compared with the thermal conduction. The calculated arc efficiency for heating the anode is 88 pct, which is in good agreement with previous measurements.[35] Furthermore, the calculated energy losses by total radiation from the arc and conduction to the cathode top are also in good agreement with experiments. Hiraoka measured them experimentally for a 100-A arc with a water-cooled copper anode.[36] We calculated them for 50, 100, and 150 A arcs in the case of the copper anode. Figures 9 and 10 show the comparison between the calculated and experimental results. The radiative energy loss is suitable to the sum of energy losses by each radiation from the cathode, arc plasma, and anode. The calculated quantitative values are almost the same with his experiments. However, the results in Table II have errors of a few percents because of the numerical inaccuracies for energy balance of our converged calculations.

Figure 11 shows the distributions of heat intensity, current density, and temperature at the anode surface in the case of the same conditions as Figures 5 and 6. Each distribution is compared with a distribution in the case of a water-cooled copper anode. The maximum heat intensity in the case of SUS304 is about 2500 W/cm^2, and it is about 57 pct of the maximum heat intensity in the case of the copper anode. In the current density distribution, the maximum of SUS304 is only 50 pct of that of the copper anode, but the distribution of SUS304 is expanded in the radial direction as compared

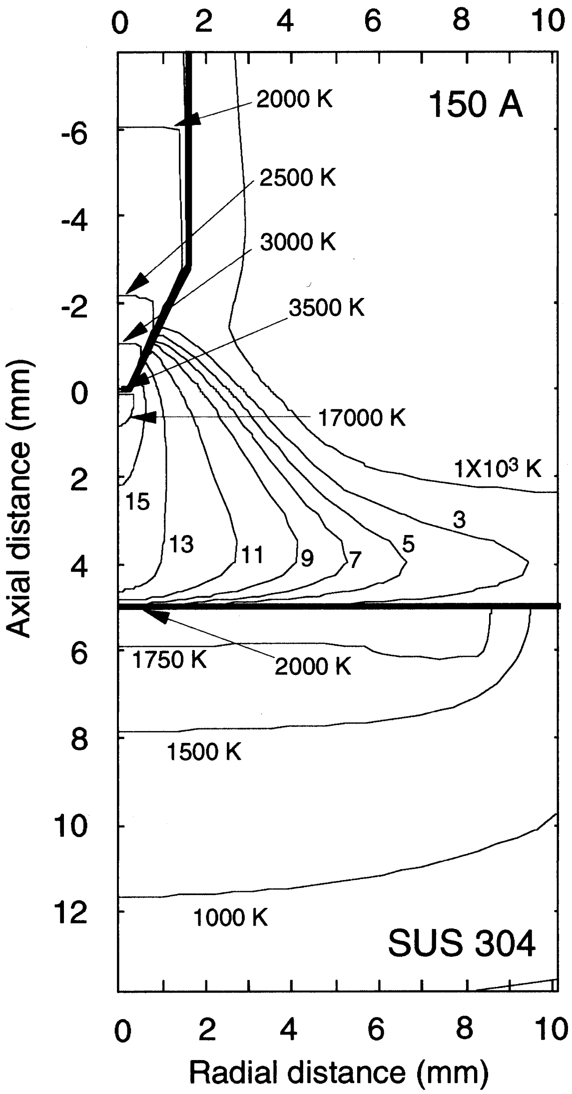

Fig. 5—Calculated temperature contours for a 150 A in stationary TIG welding of SUS304.

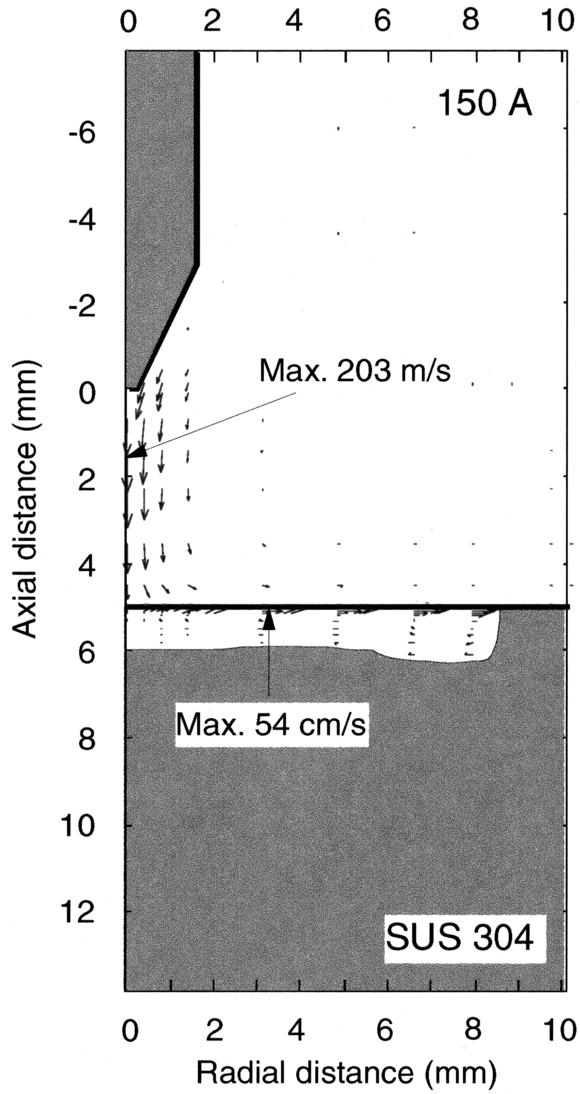

Fig. 6—Calculated fluid flow velocity for a 150 A in stationary TIG welding of SUS304.

with that of the copper anode, owing to the consistency of the same welding current. The temperature of the anode surface in the case of SUS304 is much higher than the temperature in the case of the copper anode. Figure 11 suggests that different anode materials should lead to the large differences in heat transfer from the arc plasma to the anode surface because of the close interaction between the arc plasma and the anode. Applying these numerical results of the anode heat transfer to the boundary conditions of numerical modeling only of the weld pool is necessary to take careful discussion on different materials.

A comparison of the calculated temperature contours with experimental values of our previous article[25] is made in Figure 12. The experiment for a 150, A arc with a water-cooled copper anode was carried out by laser-scattering measurement. It is seen that the predicted maximum temperature, as well as the other temperatures, are in good agreement with the experiment. Figure 13 shows the surface temperature of the cathode compared with the experimental values of Zhou and Heberlein.[37] It is also seen that the predicted temperature is in good agreement with the experiment.

Figure 14 shows the calculated weld penetration compared with experimental result. The experiment was made for 20 seconds of arcing in the same conditions as the calculation. There is approximate agreement between the calculated and experimental geometric shapes of weld penetration, although there is a difference between the calculated and experimental volumes of the weld. It is possible that the differences of physical properties taken from the literature[29–31] of thermal conductivity, specific heat, and viscosity as a function of temperature, particularly for the liquid metal, and those of the SUS304 used in our experiment would account for the differences in penetration volume. One of the other possibilities is a change in the physical properties of the weld, owing to evaporation during the arcing. The arc plasma should change a chemical composition in the weld penetration because of evaporation from the weld-pool surface, and then the physical properties of the weld would be changed. It is well known that the slight increase of surface active ele-

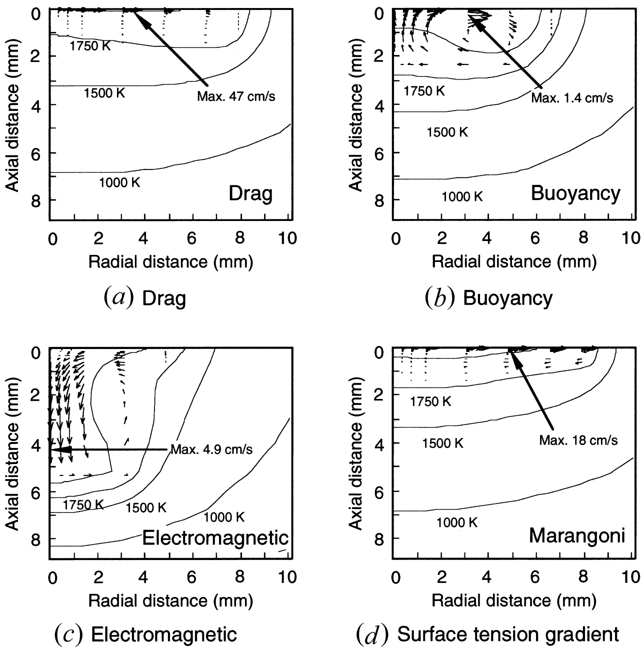

Fig. 7—(*a*) through (*d*) Temperatures and fluid flow velocities in the welds for individual driving forces corresponding to Fig. 1.

Table II. Calculated Quantitative Values of Energy Balance for Various Plasma and Electrode Regions in Stationary TIG Welding Process

Energy balance (W)			
Total heating in TIG welding (Welding current: 150 A, welding voltage: 8.1 V)			1215
At cathode	input	ohmic heating	47
		conduction from arc	478
		neutralization of ion	156
	output	thermionic emission	678
		conduction to top	33
		radiation	47
At arc plasma	input	ohmic heating	1183
	output	conduction to cathode	478
		neutralization of ion at cathode	156
		energy loss by conduction	5
		energy loss by radiation	276
		conduction to anode	373
At anode	input	ohmic heating	1
		conduction from arc	373
		electron absorption ($j\phi$)	697
	output	conduction to bottom	1009
		radiation	30

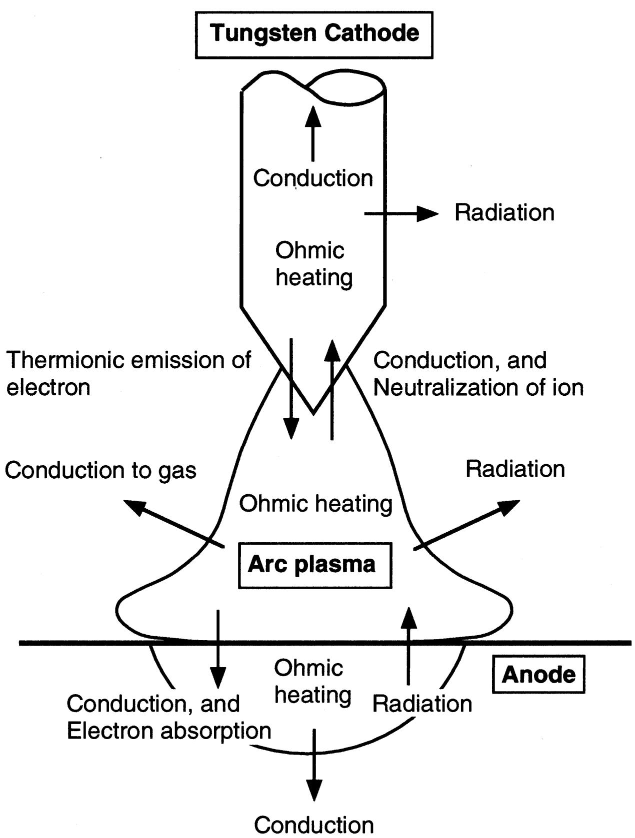

Fig. 8—Schematic illustration of energy balance in TIG welding process.

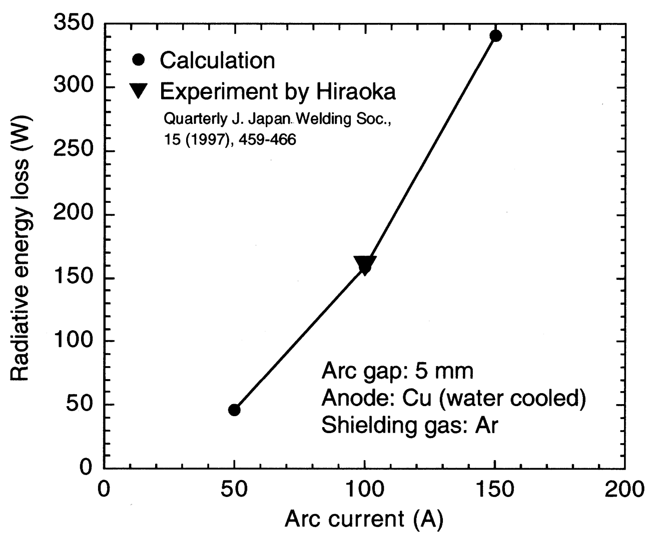

Fig. 9—Comparison of calculated energy loss by radiation from arc with experimental result of Hiraoka *et al.*[36]

ments, such as sulfur and oxygen, in the steel significantly reduces the surface tension of the molten steel.[9,10,38,39] This, in other words, means that slight evaporation of the sulfur and oxygen from the weld-pool surface would change its surface tension. Nogi experimentally showed that the evaporation of sulfur from the Fe-alloy sample clearly increased its surface tension, although the evaporation rate of sulfur from the Fe-alloy containing Cr became small.[40] As shown in Figure 7, the convective flow in the weld pool is mainly dominated by the drag force of the cathode jet and the Marangoni force. The Marangoni force, of course, is the surface-tension gradient force. The change in surface tension of the weld pool, owing to evaporation, leads to a change in the valance between the drag force of the cathode jet and the Marangoni force, and it also leads to a change in the fluid-flow velocity in the weld pool. Therefore, these changes would bring visible differences into the weld-penetration geometry. We cannot deny this evaporation effect in the present experiment, although we have taken a short time of arcing for avoiding the changes in physical properties of SUS304, owing to the evaporation. Furthermore, it is important to take account of the depression of the weld-pool surface by the arc pressure because it should change the drag force of the cathode jet at the weld-pool surface. Intensive discussion about interaction between the arc plasma and the weld pool is more necessary for solving this problem.

V. CONCLUSIONS

The conclusions in the present article are summarized as follows.

(1) The basic model and procedure in the present article was that of Sansonnens *et al.*,[16] but it was extended to include melting of the anode, with inclusion of convective effects in the weld pool.

(2) This unified numerical model of stationary TIG arc welding with the negative temperature coefficient of surface tension of molten SUS304 gave predictions of

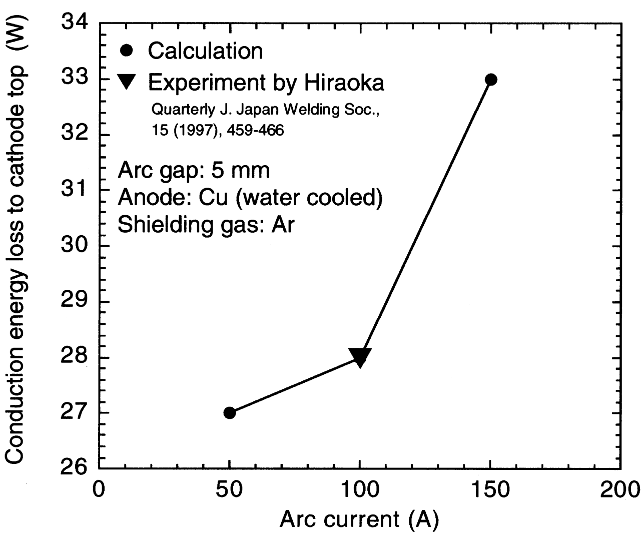

Fig. 10—Comparison of calculated energy loss by conduction to cathode top with experimental result of Hiraoka, *et al.*[36]

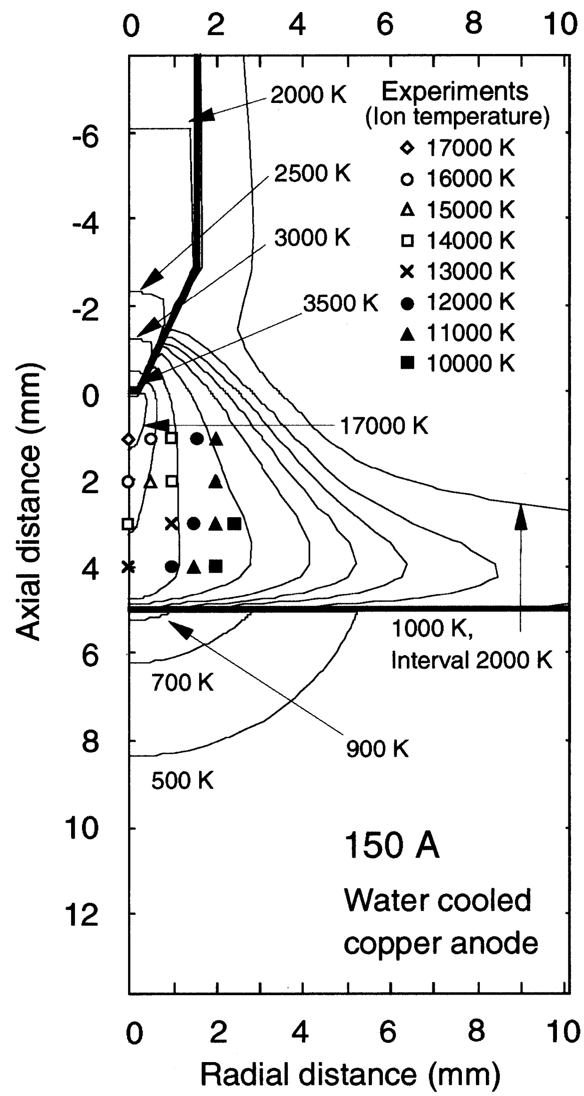

Fig. 12—Comparison of theoretical results in plasma temperature with experimental results of Tanaka.[25]

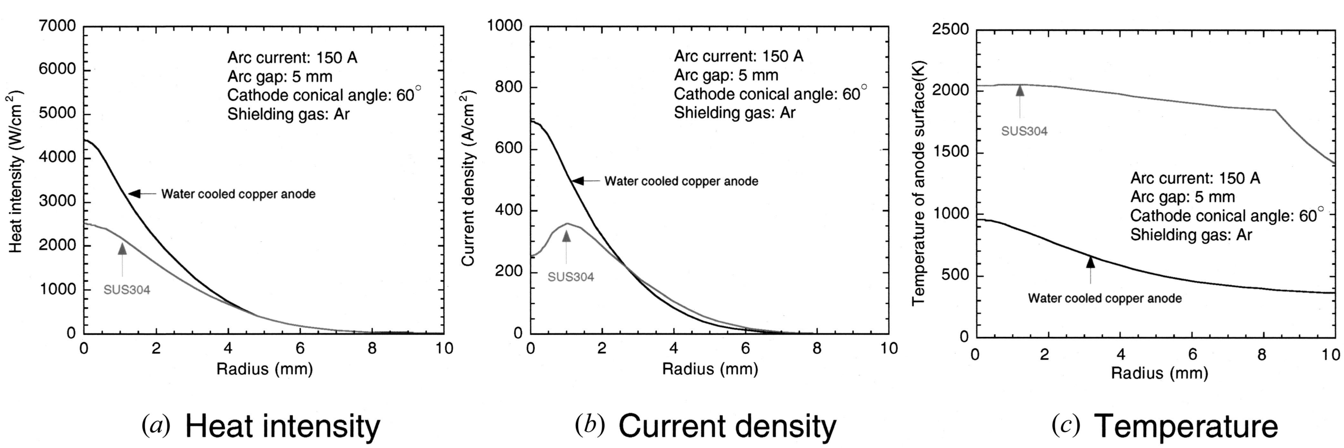

Fig. 11—Distributions of heat intensity, current density, and temperature at the anode surface of Figs. 5 and 6. (*a*) heat intensity, (*b*) current density, and (*c*) temperature.

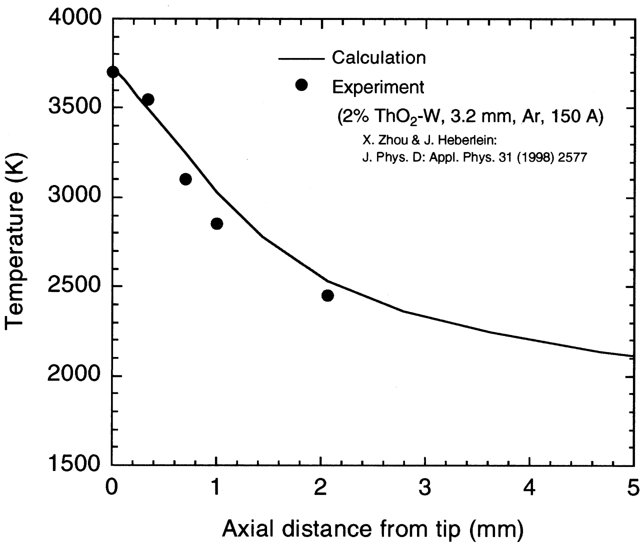

Fig. 13—Comparison of theoretical result in cathode temperature with experimental results of Zhou and Heberlein.[37]

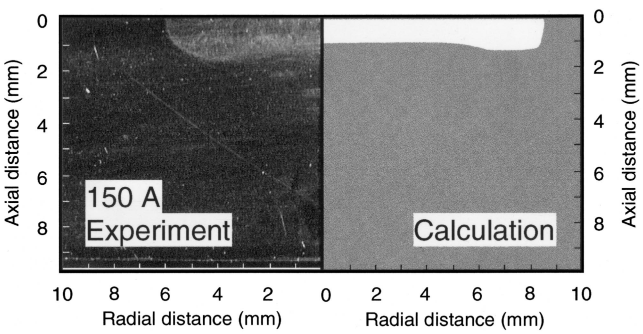

Fig. 14—Comparison of calculated result in weld penetration geometry with experimental result for a 150 A in stationary TIG welding of SUS304.

the two-dimensional distributions of temperature and velocity in the whole region of the TIG welding process, namely, tungsten cathode, arc plasma, workpiece, and weld pool. It also predicted the profile of weld penetration for a 150 A arc in argon.

(3) Furthermore, quantitative values of the energy balance for the various plasma and electrode regions were given.

(4) The predicted temperatures of the arc plasma and the tungsten-cathode surface were in good agreement with the experiments.

(5) There was also approximate agreement of the weld shape with experiment, although there was a difference between the calculated and experimental volumes of the weld. Our opinion about the possibilities of the difference was that the change in the valance between the drag force of the cathode jet and the Marangoni force, because of the depression of the weld-pool surface by the arc pressure and the evaporation from the weld-pool surface, led to a change in the fluid-flow velocity in the weld pool. This difference would lead to the differences in the heat and mass transfer in the weld pool and then bring visible differences into the weld-penetration geometry.

(6) The calculated maximum velocities of the weld pool for each driving force, namely, drag, buoyancy, electromagnetic force, and Marangoni force were 47, 1.4, 4.9, and 18 cms^{-1}, respectively. It was concluded that the convective flow in the weld pool was mainly dominated by the drag force of the cathode jet and the Marangoni force as compared with other two driving forces.

REFERENCES

1. M. Tanaka, T. Shimizu, H. Terasaki, M. Ushio, F. Koshi-ishi, and C.L. Yang: *Sci. Technol. Weld. Join.*, 2000, vol. 5, pp. 397-402.
2. A. Matsunawa: *Proc. 3rd Int. Conf. on Trends in Welding Research*, Gatlinburg, TN, June 1–5, ASM International, OH, 1992, pp. 3-16.
3. K.C. Hsu and E. Pfender: *J. Appl. Phys.*, 1983, vol. 54, pp. 4359–66.
4. P. Kovitya and J.J. Lowke: *J. Phys. D: Appl. Phys.*, 1985, vol. 18, pp. 53-70.
5. M. Ushio, J. Szekely, and C.W. Chang: *Ironmaking and Steelmaking*, 1981, vol. 6, pp. 279-86.
6. J.J. Lowke, P. kovitya, and H.P. Schmidt: *J. Phys. D: Appl. Phys.*, 1992, vol. 25, pp. 1600-06.
7. C.S. Wu, M. Ushio, and M. Tanaka: *Comput. Mater. Sci.*, 1997, vol. 7, pp. 308-14.
8. M. Goodarzi, R. Choo, and J.M. Toguri: *J. Phys. D: Appl. Phys.*, 1997, vol. 30, pp. 2744-56.
9. T. Zacharia, S.A. David, J.M. Vitek, and T. DebRoy: *Metall. Trans. B*, 1990, vol. 21B, pp. 600-03.
10. S.A. David, T. DebRoy, and J.M. Vitek: *MRS Bull.*, 1994, vol. 19, pp. 29-35.
11. T. Zacharia, S.A. David, J.M. Vitek, and H.G. Kraus: *Weld. J.*, 1995, vol. 74, pp. 353s-62s.
12. Y. Lei, Y. Shi, H. Murakawa, and Y. Ueda: *Trans. JWRI*, 1992, vol. 26, pp. 1-8.
13. C. Winkler, G. Amberg, H. Inoue, T. Koseki, and M. Fuji: *Sci. Technol. Welding Joining*, 2000, vol. 5, pp. 8-20.
14. R.T.C. Choo and J. Szekely: *Weld. J.*, 1992, vol. 71, pp. 77s-93s.
15. M. Goodarzi, R. Choo, T. Takasu, and J.M. Toguri: *J. Phys. D: Appl. Phys.*, 1998, vol. 31, pp. 569-83.
16. L. Sansonnens, J. Haidar, and J.J. Lowke: *J. Phys. D: Appl. Phys.*, 2000, vol. 33, pp. 148-57.
17. M. Tanaka, M. Ushio, and C.S. Wu: *J. Phys. D: Appl. Phys.*, 1999, vol. 32, pp. 605-11.
18. R.S. Devoto: *Phys. Fluids*, 1967, vol. 10, pp. 354-64.
19. R.S. Devoto: *Phys. Fluids*, 1967, vol. 10, pp. 2105-112.
20. M.I. Hoffert and H. Lien: *Phys. Fluids*, 1967, vol. 10, pp. 1769-77.
21. E. Hinnov and J.G. Hirschberg: *Phys. Rev.*, 1962, vol. 125, pp.795-801.
22. M.H. Hirsh and H.J. Oskam: *Gaseous Electronics*, Academic Press, New York, NY, 1978.
23. N.A. Sanders and E. Pfender: *J. Appl. Phys.*, 1984, vol. 55, pp. 714-22.
24. M. Tanaka and M. Ushio: *J. Phys. D: Appl. Phys.*, 1999, vol. 32, pp. 906-12.
25. M. Tanaka and M. Ushio: *J. Phys. D: Appl. Phys.*, 1999, vol. 32, pp. 1153-62.
26. V.M. Lelevkin, D.K. Otorbaev, and D.C. Schram: *Physics of Non-Equilibrium Plasmas*, North-Holland, Amsterdam, 1992.
27. M. Ushio, D. Fan, and M. Tanaka: *J. Phys. D: Appl. Phys.*, 1994, vol. 27, pp. 561-66.
28. S.V. Patanker: *Numerical Heat Transfer and Fluid Flow*, Hemisphere Publishing Corporation, New York, NY, 1980.
29. J.F. Elliott and M. Gleiser: *Thermochemistry for Steelmaking*, Addison-Wesley, New York, NY, 1960, vol. 1.
30. *Databook for Metals*, The Japan Institute of Metals, Maruzen, Tokyo, 1984 (in Japanese).
31. *Handbook of Stainless Steel*, Japan Stainless Steel Association, The Nikkan Kogyo Shimbun, Tokyo, 1995 (in Japanese).
32. M.I. Boulos, P. Fauchais, and E. Pfender: *Thermal Plasmas*, Plenum Press, New York, NY, 1994, vol. 1.
33. S.C. Snyder and R.E. Bentley: *J. Phys. D: Appl. Phys.*, 1996, vol. 29, pp. 3045-49.
34. J.F. Lancaster: *The Physics of Welding*, Pergamon Press, Oxford, United Kingdom, 1984.

35. W.H. Giedt, L.N. Tallerico, and P.W. Fuerschbach: *Weld. J.* 1989, vol. 68, pp. 28s-32s.
36. K. Hiraoka, N. Sakuma, and J. Zijp: *Q. J. Jpn. Weld. Soc.*, 1997, vol. 15, pp. 459-66 (in Japanese).
37. X. Zhou and J. Heberlein: *J. Phys. D: Appl. Phys.*, 1998, vol. 31, pp. 2577-90.
38. T. Zacharia, S.A. David, J.M. Vitek, and T. DebRoy: *Weld. J.*, 1989, vol. 68, pp. 499s-509s.
39. K. Ogino, K. Nogi, and C. Hosoi: *Tetsu-to-Hagané*, 1983, vol. 69, pp. 1989-94 (in Japanese).
40. K. Nogi, W.B. Chung, A. McLean, and W.A. Miller: *Mater. Trans. JIM*, 1991, vol. 32, pp. 164-68.